ROYAL SOCIETY OF CHEMISTRY

PAPER

Check for updates

Impact of bismuth-doping on enhanced radiative recombination in lead-free double-perovskite nanocrystals†

Xiaoyu Huang, [ID] [ab] Yoshitaka Matsushita, [ID] [c] Hong-Tao Sun [ID] [a] and Naoto Shirahata [ID] *[abd]

Lead-free double-perovskite nanocrystals (NCs) have received considerable attention as promising candidates for environmentally friendly optical applications. Furthermore, double-perovskite nanostructures are known to be physically stable compared to most other inorganic halide perovskites, with a generic chemical formula of ABX_3 (*e.g.*, $A = Cs^+$; $B = Sn^{2+}$ or Ge^{2+}; $X = Cl^-$, Br^-, I^-, or their combination). However, relevant experimental studies on the photophysical properties are still insufficient for Pb-free double-perovskite NCs. Herein, we synthesized $Cs_2Ag_{0.65}Na_{0.35}InCl_6$ NCs doped with bismuth (Bi^{3+}) ions and investigated their photophysical properties to reveal the role of the dopant on the enhanced photoemission properties. Specifically, it was found that the photoluminescence quantum yield (PLQY) increased up to 33.2% by 2% Bi-doping. The optical bandgap of the NCs decreased from 3.47 eV to 3.41 eV as the amount of the dopant increased from 2% to 15%. To find out the effect of Bi-doping, the temperature-dependent PL properties of the undoped and doped NCs were investigated by utilizing steady-state and time-resolved PL spectroscopy. With increasing the temperature from 20 K to 300 K, the PL intensities of the doped NCs decreased slower than the undoped ones. The correlated average PL lifetimes of both the bismuth-doped and undoped NCs decreased with increasing the temperature. The experimental results revealed that all the NC samples showed thermal quenching with the temperature increasing, and the PL quenching was suppressed in bismuth-doped NCs.

1. Introduction

Lead halide perovskite (LHP) nanocrystals (NCs) $APbX_3$ (A = Cs^+, $CH_3NH_3^+$ or $NH_2HCNH_2^+$, X = Cl^-, Br^- or I^-) have become up-and-coming materials in various optoelectronic applications, including light-emitting devices,[1–6] solar cells,[7–12] photodetectors,[13–17] photocatalysis,[18–20] and lasers,[21–23] which is attributed to their distinguished optical and electrical properties, such as high defect tolerance,[24,25] high photoluminescence (PL) quantum yield (QY),[26–28] tunable bandgap,[29,30] high color purity,[31,32] high carrier mobility, large diffusion length,[33] and high absorption coefficient,[34] as well as solution processability.[35,36] Despite the many above-mentioned advantages, the toxicity and instability of lead halide perovskite NCs are still a concern and represent a non-negligible hindrance toward their practical applications.[37,38]

To surmount these obstacles, stable and environmentally friendly perovskite compositions are urgently desired. To replace Pb^{2+}, the obvious approach is to use Sn^{2+} and Ge^{2+} because of their similar electronic properties.[39,40] However, Sn^{2+}- and Ge^{2+}-based halide perovskites are quite unstable and are easily oxidized to Sn^{4+} and Ge^{4+}. Additionally, trivalent cations Bi^{3+} and Sb^{3+} halide perovskites have also been studied,[41] but compounds with the chemical formula $A_3B_2X_9$ have shown unfavorable properties, such as a large bandgap and low defect tolerance.[42] In particular, replacing two Pb^{2+} ions with a combination of monovalent and trivalent cation could be one solution for forming three-dimensional (3D) perovskite structures, whose chemical formula is $A_2B(I)B(III)X_6$, which is called the double-perovskite structure. For instance, $Cs_2AgBiCl_6$ and $Cs_2AgInCl_6$ compounds have shown good photophysical characteristics after effective alloying or doping engineering.[43,44]

Among the reported lead-free double-perovskite materials, it has been reported recently that the bulk crystals of alloyed $Cs_2Ag_xNa_{1-x}InCl_6$:Bi double perovskites show a high PLQY of 86 ± 5% with self-trapped exciton (STE) emitting warm white
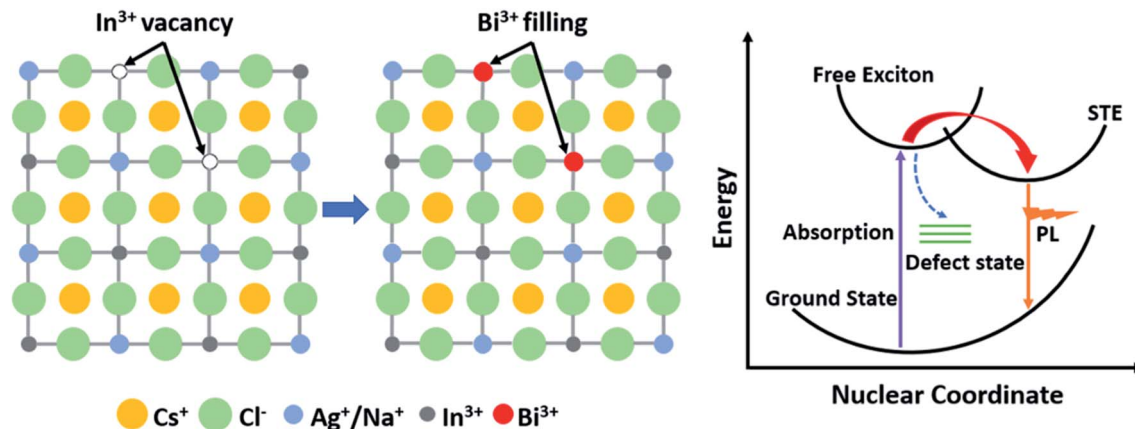
[a] International Center for Materials Nanoarchitectonics (MANA), National Institute for Materials Science (NIMS), Ibaraki 305-0044, Japan. E-mail: SHIRAHATA.Naoto@nims.go.jp

[b] Graduate School of Chemical Sciences and Engineering, Hokkaido University, Sapporo 060-0814, Japan

[c] Research Network and Facility Services Division, National Institute for Materials Science (NIMS), Ibaraki 305-0047, Japan

[d] Department of Physics, Chuo University, Tokyo 112-8551, Japan

† Electronic supplementary information (ESI) available. See https://doi.org/10.1039/d2na00238h

Scheme 1 Schematic diagram of the Bi-doping effect and proposed self-trapped emission.

light.[45] STE is normally formed by fast self-trapped excitons in materials that possess a soft lattice and strong exciton-coupling characteristics, such as halide crystals[46] and organic molecular crystals,[47] wherein the excitons relax back to the ground state by emitting photons with a broad band and large Stokes shift after being trapped; therefore the emission energy of an STE is smaller than the bandgap (Scheme 1).[48] In 2022, Bi^{3+}-doped $Cs_2Ag_{0.4}Na_{0.6}InCl_6$ microcrystals (~ 10 μm) with a remarkable high PLQY of 97.33% were achieved by Peng *et al.* through a precipitation approach.[43] Since then, double-perovskite NCs have also become a potential material for single-emitter layers applied in optical applications.[49]

Colloidal perovskite NCs terminated with surfactant ligands for high dispersibility in non-polar solvents are promising for optoelectronic applications, due to their convenient deposition on substrates based on solution processes.[50] Thereafter, for further enhancing the practicality in applications, there are efforts being directed toward the colloidal synthesis of double-perovskite NCs.[51–53] More recently, Hu *et al.* synthesized white light-emitting $Cs_2Ag_{0.17}Na_{0.83}In_{0.88}Bi_{0.12}Cl_6$ NCs with a PLQY of 64% by elemental ratio optimization and ligand passivation.[54] In the double-perovskite structure system, it has been reported that Bi-doping is responsible for the increased PLQY.[51,55,56] For the underlying mechanism of improving the PLQY through doping bismuth, there are several reported viewpoints: one is defect passivation as proved by the comparison of PL lifetimes, and another is that exciton localization is promoted after Bi-doping, which was concluded from theoretical simulations.[45] Theory predicts the radiative recombination of photogenerated carriers in the Bi–Ag centers providing that the Bi cations are present in only a small amount.[53] However, understanding and designing the experimentally fundamental photophysical properties of Bi-doped double-perovskite NCs, which could be favorable for understanding the doping effect, are still challenging themes.

A temperature-dependent PL study was established to discuss the nonradiative relaxation processes and electron–phonon interactions in the quantum dots of semiconductors.[57–59] In the present study, we used the temperature-dependent PL approach to reveal the possible excitation and emission mechanism arising from the doping of Bi^{3+} ions in $Cs_2Ag_{0.65}Na_{0.35}InCl_6$ NCs. Changes in the PL intensity and linewidth as a function of temperature were measured to gain insights into the carrier relaxation and electron–phonon coupling processes. Additionally, the temperature-dependent time-resolved PL spectra of the NCs were measured. Furthermore, the structural characterizations of the NCs at different temperatures were analyzed by the low-temperature X-ray diffraction (LT-XRD) technique to clarify the crystal-phase condition with varying the temperature.

2. Experimental

2.1 Reagents and chemicals

All the reagents were used without further purification. Cesium acetate (CsOAc, 99.99%), silver acetate (AgOAc, 99%), sodium acetate (NaOAc, 99.99%), indium(III) acetate (In(OAc)$_3$, 99.99%), bismuth(III) acetate (Bi(OAc)$_3$, 99.99%), chlorotrimethylsilane (TMSCl, 98%), oleic acid (OA, 90%), and 1-octadecane (ODE, 95%) were purchased from Sigma-Aldrich. Oleylamine (OAm, 80–90%) was purchased from Kanto Kagaku. Toluene (99.5%), hexane (96%), and ethyl acetate (99.5%) were purchased from Wako Chemicals.

2.2 Preparation of $Cs_2Ag_{0.65}Na_{0.35}In_{1-x}Bi_xCl_6$ NCs

The NCs were fabricated following a modified version of the hot-injection method reported by Han and co-workers.[52] In a typical synthesis, 1.3 mmol CsOAc, 0.36 mmol AgOAc, 0.54 mmol NaOAc, 1.98 mmol In(OAc)$_3$, and 0.02 mmol Bi(OAc)$_3$ were loaded in a 50 mL three-neck flask containing 5.6 mL OA, 1.4 mL OLA, and 20 mL ODE, after degassing for 1 h at 110 °C, and then heated to 165 °C in 12 min under a N$_2$ flow. Next, 0.8 mL TMSCl was injected quickly, with the temperature increasing for 2 min longer, and then the production was rapidly cooled down to 25 °C by placing in an ice-water bath. The resultant NCs were centrifuged at 9000 rpm for 20 min and washed with toluene to remove any unreacted precursors. Then, the collected precipitate was further dispersed in hexane, and

thereafter the resultant solution was centrifuged at 6000 rpm for 15 min and the supernatant was collected. The same volume of ethyl acetate was added for the final centrifugation, and the final precipitate was collected and vacuum-dried for further characterization.

2.3 Characterization

The powder samples with different Bi-doping amounts were analyzed using a JASCO V-650 UV-visible spectrometer. High-resolution transmission electron microscopy (HR-TEM) characterization was performed using a JEM-2100F2 instrument (JEOL) at 200 kV acceleration voltage. Scanning transmission electron microscopy energy dispersive spectroscopy (STEM-EDS) was utilized for the element analysis. Samples for the TEM analysis were prepared by drop-casting the 0.1 mg mL^{-1} hexane solution of NCs onto carbon-coated copper grids. PLQYs were measured at room temperature using the absolute PLQY spectrometer C11347-11 from Hamamatsu Photonics Co. Ltd with a 150 W xenon light source coupled to a monochromator for wavelength discrimination, an integrating sphere as a sample chamber, and a multichannel spectroscope for signal detection. The powder forms of the specimens of NCs were used for the characterization of the PLQY. The PL properties were

measured with the powder samples pressed and coated onto the interlayer between two 1 cm × 1 cm quartz glasses. Measurements were conducted using a modular double-grating Czerny–Turner monochromator and an iHR 320 emission monochromator (1200 lines per mm of gratings) coupled to a photodetector on a NanoLog Horiba Jobin Yvon spectrofluorometer with a 450 E Xe arc lamp. The value of photon power for the excitation estimated using a power meter (PD 300, Ophir Optronics Solutions Ltd and NOVA II display) was 0.014 mW cm^{-2}. To measure the temperature-dependent PL spectra, the samples were placed inside a cryostat holder connected to a Gifford–McMahon cooler and controlled by a Mercury iTC temperature controller. The temperature was tuned from 3 K to 300 K with 20 K per step. The LT-XRD characterization in the temperature range between 5 K and 300 K was carried out using a Rigaku SmartLab system (9 kW, Cu Kα$_1$) equipped with a cryostat attachment, where the sample was tightly attached using Apiezon-N grease on a copper sample holder.

3. Results and discussion

Bi-doped and undoped $Cs_2Ag_{0.65}Na_{0.35}InCl_6$ NCs were synthesized by the modified hot-injection method.[52] Here, PeNC$_0$, PeNC$_1$, and PeNC$_{10}$ represent $Cs_2Ag_{0.65}Na_{0.35}InCl_6$ double-

Fig. 1 Crystal structure of $Cs_2Ag_{1-x}Na_xIn_{1-y}Bi_yCl_6$ double perovskite. Yellow, silver, purple, and green spheres represent Cs, Ag/Na, In/Bi, and Cl atoms, respectively. (b) X-ray diffraction (XRD) patterns measured at room temperature of PeNC$_x$ ($Cs_2Ag_{0.65}Na_{0.35}In_{1-x\%}Bi_{x\%}Cl_6$, x = 0, 1, 10) and the enlarged XRD patterns of the samples between 23° and 25°. Transmission electron microscopy (TEM) images of (c) PeNC$_0$, (d) PeNC$_1$, and (e) PeNC$_{10}$. The scale bar is 20 nm. The inset in the top-right corner is the high-resolution TEM image, whose scale bar is 5 nm. The inset in the bottom right corner is the size-distribution histogram.

perovskite NCs with 0%, 1%, and 10% Bi precursor concentration, respectively. The STEM-EDS analysis revealed that the final products of $PeNC_1$ and $PeNC_{10}$ had 2% and 15% Bi. It should be noted that all the composition values stand for the actual value for the results that we obtained from STEM-EDS as listed in Table S1.† The atom ratios of Cs/In and Cl/In showed the ranges of 2.32–2.48 and 4.86–5.61, respectively. This deviation with the feeding ratio was reasonable compared with other double-perovskite nanocrystals.[60,61] On the one hand, the large ratio of Cs/In might be caused by the indium vacancies in this structure, and this ratio decreased with the increasing bismuth amount. Meanwhile, the elemental ratio deviation was also found in $Cs_2AgBiCl_6$, whereas the ratios were 2.25 and 20 for Cs/Ag and Cl/Ag, respectively.[60] However, the cause of the large ratio on Cl/In has not been clearly clarified yet, and needs to be investigated in future work. HR-TEM images of $Cs_2Ag_{0.65}-Na_{0.35}InCl_6$ NCs showed that the crystals had a cubic structure. As shown in Fig. 1c–e, the average sizes of $PeNC_0$, $PeNC_1$, and $PeNC_{10}$ were 10.45 ± 1.97, 10.03 ± 1.72, and 10.01 ± 1.68 nm, respectively. Their sizes were quite close to each other. Based on that, the particle size difference was not considered in the subsequent discussion of the optical properties. Additionally, the corresponding measured lattice distances were 3.71, 3.71, and 3.63 Å, which were in accord with the (220) planes in $Cs_2-Ag_{0.65}Na_{0.35}InCl_6$ NCs, as shown by XRD in the following part. The XRD patterns of $Cs_2Ag_{0.65}Na_{0.35}InCl_6$ NCs matched well with the cubic double-perovskite structure ($Cs_2AgInCl_6$ ICSD code 1546186, $Cs_2NaInCl_6$ ICSD code 4003575) in all three samples, and no impurity phases were observed (see Fig. 1b), which demonstrated the good phase stability of the $Cs_2Ag_{0.65}-Na_{0.35}InCl_6$ double-perovskite. Comparing the XRD pattern of $PeNC_1$ with that of $PeNC_{10}$, we could see a small shift of the 220 peak from 23.9° to 23.8° with increasing the bismuth amount from 2% to 15%, which was possibility due to the lattice expansion resulting from the substitution of Bi^{3+} ions (117 pm) for In^{3+} ions (92 pm) in the cubic lattice.[62] $Cs_2Ag_{0.65}Na_{0.35}InCl_6$ NCs with a higher concentration of Bi-dopant were also synthesized, and the lattice parameters of NCs as a function of the Bi-dopant concentration (see Fig. S1†) were investigated, which showed that when the Bi amount increased, the crystal

structure of the NCs obeyed Vegard's law,[63] and there was no impurity phase or phase separation.

It is common that structural phase transition happens in lead halide perovskite NCs under low temperature, which is caused by size effects or doping effects.[64–66] A phase transition from tetragonal- to cubic structures has been observed at 122 K for $Cs_2AgBiBr_6$ which is one of the double-perovskite crystals.[67] Such a temperature-dependent phase transition influences adversely the device performance in some cases. To investigate the structural stability of the $Cs_2Ag_{0.65}Na_{0.35}InCl_6$ NCs when the temperature varies, LT-XRD measurements were performed. For the LT-XRD measurements between 5 K and 300 K, the $PeNC_0$, $PeNC_1$, and $PeNC_{10}$ samples were selected (see Fig. 2a–c). All the LT-XRD patterns of the doped samples were found to be similar to that of the undoped sample. The absence of additional peaks appeared over the whole temperature range for the doped samples. This indicates that the phase stayed in the cubic phase, implying a good crystallinity and purity. At 5 K, when the Bi amount increased to 2%, the diffraction lines of the $PeNC_1$ showed a relative shift compared to that of the $PeNC_0$, with the 15% Bi-doped $PeNC_{10}$ showing a 0.22° smaller shift than $PeNC_0$, which was consistent with the characteristics shown at room temperature (see Fig. S2†). On the temperature dependence, all the XRD peaks shifted toward a smaller diffraction angle with increasing the temperature, possibly due to a lattice expansion. The experimental data of the lattice constant were fitted by a second-order polynomial, as shown in Fig. S3.† The linear coefficient of thermal expansions for $PeNC_0$, $PeNC_1$, and $PeNC_{10}$ was found to be 1.71×10^{-5}/K, 1.27×10^{-5}/K, and 1.52×10^{-5}/K, respectively. The results from these calculations indicated that the doped sample changed slowly with temperature, which would permit high thermal stability for their target applications.

The optical properties of $Cs_2Ag_{0.65}Na_{0.35}InCl_6$ NCs were studied by UV-Vis and PL spectroscopies. Also, the resultant optical absorption and PL spectra of the $Cs_2Ag_{0.65}Na_{0.35}InCl_6$ NC samples were determined and are shown in Fig. 3. Cation doping has complicated impacts on the perovskite nanocrystals because even a very small substitution of In^{3+} by Bi^{3+} would greatly affect the bandgap and exciton radiation channel. For the undoped sample $PeNC_0$, the conduction band minimum
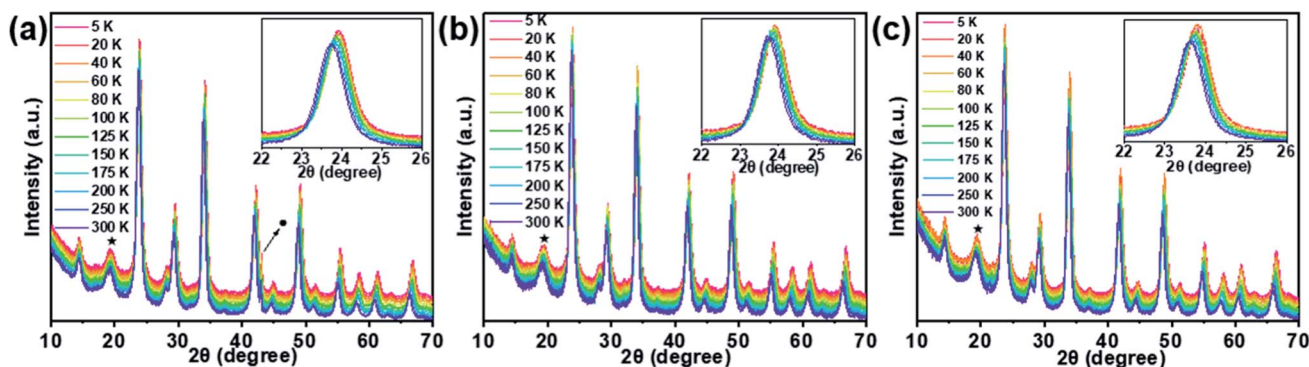

Fig. 2 LT-XRD patterns of (a) $PeNC_0$, (b) $PeNC_1$, and (c) $PeNC_{10}$ in the temperature range from 5–300 K. Peaks indicated as ★ and ● are from the X-ray window materials of the cryostat and from the Cu sample holder, respectively.
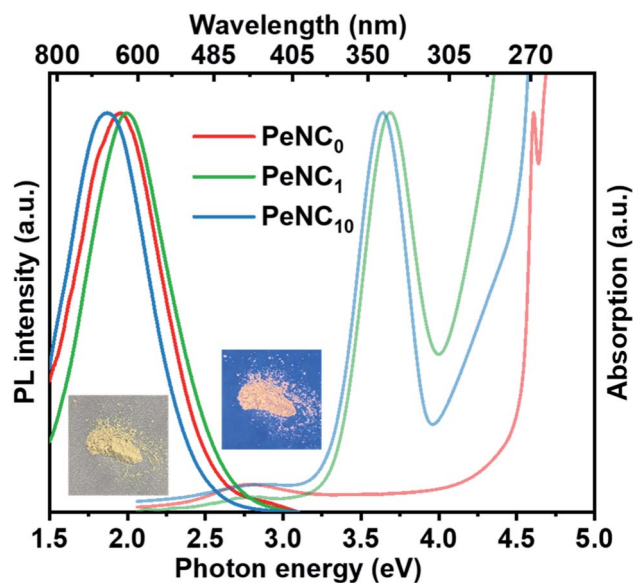
Fig. 3 UV-Vis absorption and PL spectra of PeNC$_0$ (λ_{ex} = 275 nm), PeNC$_1$ (λ_{ex} = 330 nm), and PeNC$_{10}$ (λ_{ex} = 330 nm) with nanocrystals in the powder form. Photographs showing the PeNC$_1$ powder sample under room illumination (left) and UV irradiation (right).

(CBM) was mainly contributed by In-5s and Cl-3p, and the valence band maximum (VBM) was contributed by Ag-4d and Cl-3p.[45] When Bi^{3+} ions were doped into the NCs, it was noted that an additional excitonic absorption peak was presented near 3.7 eV, which was attributed to band-edge absorption where Bi could be the localization center for electrons at the conduction band edges.[55,68] With the incremental addition of Bi ions from 2% to 15%, the optical bandgap estimated by the Tauc plots (Fig. S4†) narrowed from 3.47 eV to 3.41 eV, which was caused by the lower CBM of the p-orbital derived from Bi cations.[69] The excitation energy was obtained from the photoluminescence excitation (PLE) peak value (Fig. S5†). The PL spectrum of the PeNC$_0$ was observed by excitation with 4.51 eV, while the PL spectra of PeNC$_1$ and PeNC$_{10}$ were obtained by excitation at 3.76 eV. The red-shift in the PL spectra of PeNC$_{10}$ compared to PeNC$_1$ corresponded to the narrowed bandgap. The highest PLQY of 33.2% was observed for PeNC$_1$, while it was 3% for PeNC$_0$ and 15.5% for PeNC$_{10}$ as shown in Table 1 and Fig. S6.†

To discuss a possible mechanism of the doping effect on the PL performance, the PL spectra of PeNC$_0$, PeNC$_1$, and PeNC$_{10}$ in powder form were measured in the temperature range between 20 K to 300 K. Fig. 4 shows the variation in the PL spectra of

PeNC$_0$, PeNC$_1$ and PeNC$_{10}$ photoexcited at 4.51, 3.76, and 3.76 eV, respectively. It is worth mentioning that there was a weak peak at around 2.76 eV for the PeNC$_0$ (see Fig. 4a), which could be attributed to the free-exciton emission.[45] Fig. 4a–c shows the decreasing trend in the PL intensity of all the three samples with the temperature rise. Meanwhile, the samples exhibited a red-shift in the PL peak when the temperature was increased from 20 K to 100 K. Interestingly, this behavior is the opposite of most reported perovskite NCs.[64,70–72] There are a few papers showing a red-shift trend, but those crystals are known to show the temperature-dependent phase transition or halide-type effect.[63,73] However, the results of the LT-XRD measurements showed that all three samples maintained an ideal cubic perovskite structure and unchanged crystal phase in the temperature range between 5 K and 300 K. As mentioned before, the broad emission of the Cs$_2$Ag$_{0.65}$Na$_{0.35}$InCl$_6$ NCs originated from STE emission. Herein we propose that the red-shift of the PL peak could be attributed to the narrowing emission bandgap of the self-trapped state with the temperature increasing, which resulted from the lattice dilatation and electron–phonon interaction, similar to conventional semiconductor materials.[74]

The variation in the PL peak energy with temperature from 20 K to 300 K for the three samples is shown in Fig. 5a. The PL peak energies of the NC powders for PeNC$_0$, PeNC$_1$, and PeNC$_{10}$ were determined to be 2.00, 2.05, and 1.90 eV at 20 K and 1.93, 2.00, and 1.87 eV at 300 K, respectively. It was seen that the PL peak energy of PeNC$_0$ decreased significantly (0.25 meV K^{-1}) while the other two doped samples (i.e. PeNC$_1$ and PeNC$_{10}$) exhibited smaller shifts of 0.18 and 0.11 meV K^{-1} with the increasing temperature. On the other hand, the integrated PL intensities for the PeNC$_0$, PeNC$_1$, and PeNC$_{10}$ samples slightly decreased with the increasing temperature as shown in Fig. 5b, yielding PL quenching. The successive decreasing behaviors of the PL intensity with the rise in temperature appeared due to the thermal activation of the nonradiative channels present in the NCs. According to this context, PeNC$_0$ contained the largest amounts of defects as nonradiative channels, whereas PeNC$_1$ had the smallest defect density (Scheme 1), consistent with the difference in PLQY. The temperature-dependent PL intensities could be fitted well according to the Arrhenius formula:[75]

$$I(T) = \frac{I_0}{1 + A \exp\left(-\dfrac{E_A}{K_B T}\right)} \quad (1)$$

where I_0 is the PL intensity at 20 K, A is the proportional constant, E_A is the activation energy, and K_B is the Boltzmann

Table 1 Decay parameters of the PeNCs at room temperature[a]

Sample	PLQY (%)	τ_1 (µs) (A_1%)	τ_2 (µs) (A_2%)	τ_{avg} (µs)	k_r (µs^{-1})	k_{nr} (µs^{-1})	R-Square
PeNC$_0$	3	0.23	—	0.23	0.13	4.20	0.998
PeNC$_1$	33.2	1.10 (79%)	7.26 (21%)	2.40	0.14	0.28	0.973
PeNC$_{10}$	15.5	0.81 (80%)	3.53 (20%)	1.36	0.11	0.62	0.999

[a] PLQY: photoluminescence quantum yield; τ_1-short and τ_2-long lifetime; A_1 and A_2 are the contributions for τ_1 and τ_2, respectively; τ_{avg}: average lifetime, which was calculated by $\tau_{avg} = \tau_1 A_1 + \tau_2 A_2$; k_r-radiative recombination rate and k_{nr}-nonradiative recombination rate, which were calculated by k_r = PLQY/τ_{avg} and k_{nr} = 1/τ_{avg} − k_r, respectively.
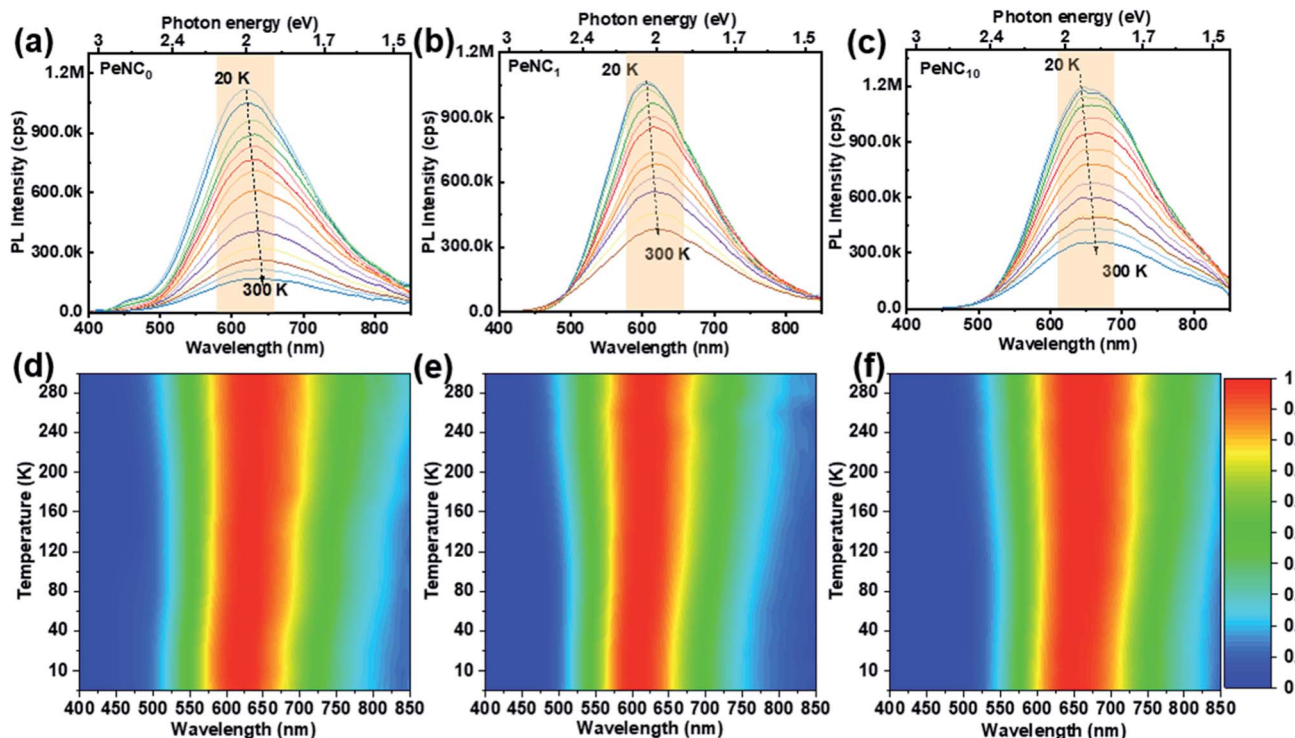
Fig. 4 Temperature-dependent PL spectra of (a) PeNC$_0$ (λ_{ex} = 275 nm), (b) PeNC$_1$ (λ_{ex} = 330 nm), and (c) PeNC$_{10}$ (λ_{ex} = 330 nm) from 20 to 300 K. Normalized PL intensity mapped with the emission wavelength and temperature for (d) PeNC$_0$ (e) PeNC$_1$, and (f) PeNC$_{10}$.

constant. The estimated values of thermal activation energy were 55.8, 46.3, and 48.8 meV for the PeNC$_0$, PeNC$_1$, and PeNC$_{10}$ samples.

It can be seen from Fig. 4d–f that the PL full-width at half maximum (FWHM) was broadened for each sample with the temperature increasing, which was attributed to the strong exciton–phonon coupling. As shown in Fig. 5c, the PL FWHM was fitted by adapting the independent Boson model:[76]

$$\Gamma(T) = \Gamma_0 + \sigma T + \frac{\Gamma_{OP}}{\exp\left(\dfrac{\hbar\omega_{OP}}{K_B T}\right) - 1} \tag{2}$$

where Γ_0 is the inhomogeneous broadening contribution, σ and Γ_{OP} describe the interactions of the exciton–acoustic phonon interaction and the exciton–optical phonon interaction contributions to the FWHM broadening, respectively, and $\hbar\omega_{OP}$ is the optical phonon energy. The corresponding fitted values are listed in Table 2, where it can be seen that the fitted optical phonon energies of PeNC$_0$, PeNC$_1$ and PeNC$_{10}$ were 47.9, 41.2, and 42.0 meV, respectively. These values were similar to the bulk phonon energy ($\sim$50 meV).[79] Smaller optical phonon energy values of the doped samples imply that more phonons are produced, which would serve as scattering centers,[77] possibly due to the strained crystalline lattice by doped ions. The inhomogeneous broadening of PL FWHM might be contributed by the surface defect-induced trap state.[78] Also, the inhomogeneous broadening factor of PeNC$_0$ (555 meV) was higher than that of PeNC$_1$ (490 meV), which indicated that the
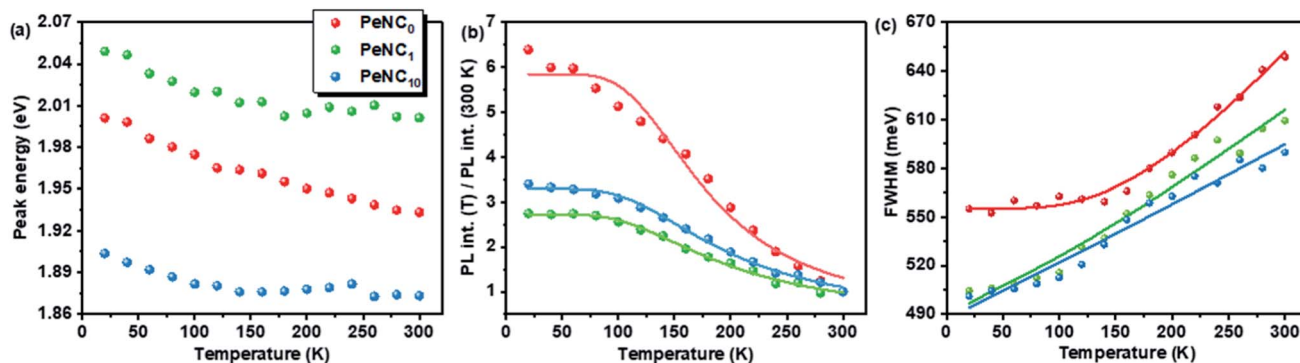

Fig. 5 Temperature-dependent PL (a) emission peak energy, (b) peak intensity, and (c) FWHM of PeNC$_0$, PeNC$_1$, and PeNC$_{10}$.

Table 2 Physical parameters obtained from fitting the experimental temperature-dependent PL data[a]

Sample	Γ_o (meV)	σ (meV K^{-1})	E_{ph} (meV)	Γ_{op} (meV)	E_A (meV)
PeNC$_0$	555.4 ± 2.2	1.33×10^{-13}	47.9	519.3 ± 22.0	55.8 ± 6.2
PeNC$_1$	489.7 ± 7.1	0.353 ± 0.069	41.2	80.3 ± 70.7	46.3 ± 2.3
PeNC$_{10}$	487.1 ± 6.0	0.345 ± 0.068	42.0	16.7 ± 72.0	48.8 ± 2.4

[a] Γ_o: inhomogeneous broadening; σ: coupling coefficient of exciton–acoustic phonons; E_{ph}: longitudinal optical (LO) phonon energy; Γ_{op}: coupling strength of exciton–LO phonons; E_A: activation energy.
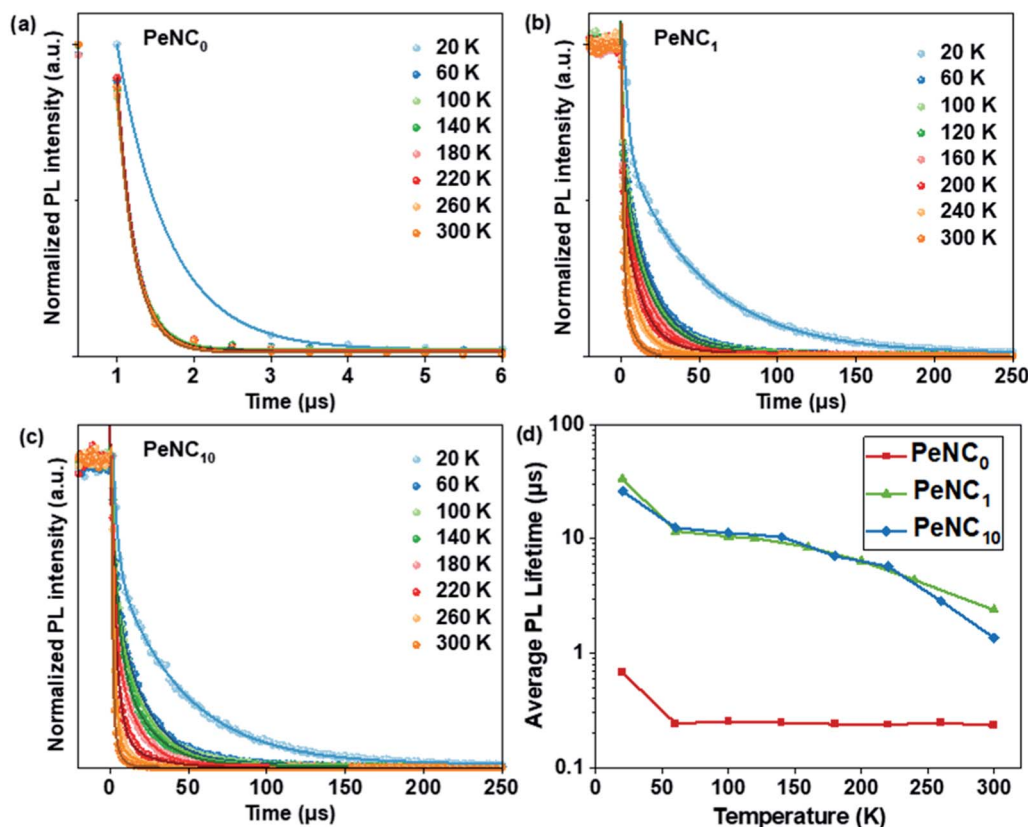

Fig. 6 TR-PL curves of (a) PeNC$_0$ (b) PeNC$_1$, (c) PeNC$_{10}$ from 20 to 300 K and (d) their average lifetimes extracted from biexponential fitting at various temperatures.

defect density was suppressed after Bi-doping. Electron–phonon coupling is also crucial to the formation of STEs, where, because of the "soft" lattice nature of the octahedral halide coordination in the double-perovskite structure, strong electron–phonon coupling results in elastic structural distortion, leading to a broadband STE emission.[48] A highly efficient radiative recombination process thus requires a suitable electron–phonon coupling effect. The electron–phonon coupling could be quantitatively characterized by Huang–Rhys' factor S. The S value is normally small in free-exciton materials, such as CdSe[80] and CsPbBr$_3$,[81] but larger than 10 in STE materials. As shown in Fig. S7,† the fitted S values for PeNC$_0$, PeNC$_1$, and PeNC$_{10}$ were 24.1, 27.7, and 26.7, respectively, which were smaller than bulk crystals ($\sim$40)[45] but larger than reported NCs (15.5).[54] It was demonstrated that Cs$_2$Ag$_{0.65}$Na$_{0.35}$InCl$_6$ NCs possessed enough electron–phonon coupling, which is beneficial for the formation of STE emission, to achieve a high PLQY.

Besides the broadband and large Stokes shift emission, a long radiative PL lifetime is also a specific property of STEs, and is shown in Fig. 6a–c. To study the effect of doped Bi on the charge-carrier lifetime as a function of temperature, we measured time-resolved PL as a function of temperature for the PeNC$_0$, PeNC$_1$, and PeNC$_{10}$ samples between 20 K and 300 K. As shown in Fig. 6d, the average lifetimes of PeNC$_1$ and PeNC$_{10}$ were longer than that of PeNC$_0$ at all the temperatures, while the short lifetime component was ascribed to the trap-assisted nonradiative recombination channel, which when combined with the calculated nonradiative recombination rate in Table 1 allows concluding that the Bi-doping passivates the defects and suppresses the nonradiative recombination rate. The temperature-dependent average lifetimes of exciton decay for the Bi-doped samples were calculated by fitting the data to a biexponential fit (Table S2†) with a long-lived component (3–50 μs) and a less-long-lived component (0.8–3 μs), while the PL

decay of undoped NCs was fitted by a mono-exponential function with a less-long-lived component (0.23 μs). The R-square values of the three plots were larger than 0.97, indicating a good fit. As shown in Fig. 6d, all three samples demonstrated that the changes in the lifetime were shortened a lot from 20 K to 60 K, but quite mild in the range from 60 K to 300 K, which could be described as the Boltzmann distribution,[82] in accordance with the reported broadband-emission double perovskites.[52] The proportion of the less-long-lived components *versus* temperature is shown in Fig. S8,† and this contribution became prominent when the temperature increased in both $PeNC_1$ and $PeNC_{10}$. Combined with the decreased PL intensity when the temperature increased, the less-long-lived component could be ascribed to fast nonradiative losses, likely due to the defects, while the long-lived part was contributed by the recombination of the STE. This phenomenon has also been observed in other double-perovskite nanocrystals.[53] As a result, the average PL lifetimes decreased with the increasing temperature due to the increasing contribution of the faster nonradiative decay channels.

4. Conclusions

We synthesized undoped and bismuth-doped $Cs_2Ag_{0.65}Na_{0.35}InCl_6$ double-perovskite NCs to investigate the role of the dopant on the enhanced PL performance through LT-XRD and low-temperature PL spectroscopic studies. The LT-XRD characterization indicated the successful doping and showed that there was no phase transition between 5 K and 300 K. The absolute value of PLQY was as high as 33.2%, which was obtained by 2% bismuth doping. The temperature-dependent PL study suggested that the diminished nonradiative channels brought about the increase in the PLQY. The PL linewidth broadening from 20 K to 300 K of the NCs was explained by electron–phonon coupling.

Author contributions

X. H. performed research; Y. M. measured the samples with XRD at different temperatures; all the authors discussed the results, and X. H. and N. S. wrote the paper.

Conflicts of interest

There are no conflicts to declare.

Acknowledgements

References

1 J. Song, J. Li, X. Li, L. Xu, Y. Dong and H. Zeng, *Adv. Mater.*, 2015, **27**, 7162–7167.

2 H. Huang, L. Polavarapu, J. A. Sichert, A. S. Susha, A. S. Urban and A. L. Rogach, *NPG Asia Mater.*, 2016, **8**, e328.

3 L. Zhao, Y.-W. Yeh, N. L. Tran, F. Wu, Z. Xiao, R. A. Kerner, Y. L. Lin, G. D. Scholes, N. Yao and B. P. Rand, *ACS Nano*, 2017, **11**, 3957–3964.

4 F. Yan, J. Xing, G. Xing, L. Quan, S. T. Tan, J. Zhao, R. Su, L. Zhang, S. Chen, Y. Zhao, A. Huan, E. H. Sargent, Q. Xiong and H. V. Demir, *Nano Lett.*, 2018, **18**, 3157–3164.

5 Y. Wei, Z. Cheng and J. Lin, *Chem. Soc. Rev.*, 2019, **48**, 310–350.

6 Y. Hassan, J. H. Park, M. L. Crawford, A. Sadhanala, J. Lee, J. C. Sadighian, E. Mosconi, R. Shivanna, E. Radicchi, M. Jeong, C. Yang, H. Choi, S. H. Park, M. H. Song, F. De Angelis, C. Y. Wong, R. H. Friend, B. R. Lee and H. J. Snaith, *Nature*, 2021, **591**, 72–77.

7 J. Yuan, X. Ling, D. Yang, F. Li, S. Zhou, J. Shi, Y. Qian, J. Hu, Y. Sun, Y. Yang, X. Gao, S. Duhm, Q. Zhang and W. Ma, *Joule*, 2018, **2**, 2450–2463.

8 Q. A. Akkerman, M. Gandini, F. Di Stasio, P. Rastogi, F. Palazon, G. Bertoni, J. M. Ball, M. Prato, A. Petrozza and L. Manna, *Nat. Energy*, 2017, **2**, 16194.

9 J. Kim, B. Koo, W. H. Kim, J. Choi, C. Choi, S. J. Lim, J.-S. Lee, D.-H. Kim, M. J. Ko and Y. Kim, *Nano Energy*, 2019, **66**, 104130.

10 J. Xi, C. Piao, J. Byeon, J. Yoon, Z. Wu and M. Choi, *Adv. Energy Mater.*, 2019, **9**, 1901787.

11 L. Hu, Q. Zhao, S. Huang, J. Zheng, X. Guan, R. Patterson, J. Kim, L. Shi, C.-H. Lin, Q. Lei, D. Chu, W. Tao, S. Cheong, R. D. Tilley, A. W. Y. Ho-Baillie, J. M. Luther, J. Yuan and T. Wu, *Nat. Commun.*, 2021, **12**, 466.

12 Y. Wang, J. Yuan, X. Zhang, X. Ling, B. W. Larson, Q. Zhao, Y. Yang, Y. Shi, J. M. Luther and W. Ma, *Adv. Mater.*, 2020, **32**, 2000449.

13 P. Ramasamy, D.-H. Lim, B. Kim, S.-H. Lee, M.-S. Lee and J.-S. Lee, *Chem. Commun.*, 2016, **52**, 2067–2070.

14 L. Zhou, K. Yu, F. Yang, J. Zheng, Y. Zuo, C. Li, B. Cheng and Q. Wang, *Dalton Trans.*, 2017, **46**, 1766–1769.

15 C. Bi, S. V. Kershaw, A. L. Rogach and J. Tian, *Adv. Funct. Mater.*, 2019, **29**, 1902446.

16 T. Zou, X. Liu, R. Qiu, Y. Wang, S. Huang, C. Liu, Q. Dai and H. Zhou, *Adv. Opt. Mater.*, 2019, **7**, 1801812.

17 L. Jin, Y. Zhang, M. Cao, Y. Yu, Z. Chen, Y. Li, Z. Zhong, X. Hua, L. Xu, C. Cai, Y. Hu, X. Tong and J. Yao, *Nanotechnology*, 2021, **32**, 235203.

18 L. Wu, Y. Mu, X. Guo, W. Zhang, Z. Zhang, M. Zhang and T. Lu, *Angew. Chem., Int. Ed.*, 2019, **58**, 9491–9495.

19 A. Pan, X. Ma, S. Huang, Y. Wu, M. Jia, Y. Shi, Y. Liu, P. Wangyang, L. He and Y. Liu, *J. Phys. Chem. Lett.*, 2019, **10**, 6590–6597.

20 Z. Chen, Y. Hu, J. Wang, Q. Shen, Y. Zhang, C. Ding, Y. Bai, G. Jiang, Z. Li and N. Gaponik, *Chem. Mater.*, 2020, **32**, 1517–1525.

21 C.-Y. Huang, C. Zou, C. Mao, K. L. Corp, Y.-C. Yao, Y.-J. Lee, C. W. Schlenker, A. K. Y. Jen and L. Y. Lin, *ACS Photonics*, 2017, **4**, 2281–2289.

22 J. Chen, W. Du, J. Shi, M. Li, Y. Wang, Q. Zhang and X. Liu, *InfoMat*, 2020, **2**, 170–183.

23 W. Gao, T. Wang, J. Xu, P. Zeng, W. Zhang, Y. Yao, C. Chen, M. Li and S. F. Yu, *Small*, 2021, **17**, 2103065.

24 S. Mandal, S. Mukherjee, C. K. De, D. Roy, S. Ghosh and P. K. Mandal, *J. Phys. Chem. Lett.*, 2020, **11**, 1702–1707.

25 J. Kang and L.-W. Wang, *J. Phys. Chem. Lett.*, 2017, **8**, 489–493.

26 J.-W. Lee, Y. J. Choi, J.-M. Yang, S. Ham, S. K. Jeon, J. Y. Lee, Y.-H. Song, E. K. Ji, D.-H. Yoon, S. Seo, H. Shin, G. S. Han, H. S. Jung, D. Kim and N.-G. Park, *ACS Nano*, 2017, **11**, 3311–3319.

27 B. A. Koscher, J. K. Swabeck, N. D. Bronstein and A. P. Alivisatos, *J. Am. Chem. Soc.*, 2017, **139**, 6566–6569.

28 N. Mondal, A. De and A. Samanta, *ACS Energy Lett.*, 2019, **4**, 32–39.

29 I. Levchuk, A. Osvet, X. Tang, M. Brandl, J. D. Perea, F. Hoegl, G. J. Matt, R. Hock, M. Batentschuk and C. J. Brabec, *Nano Lett.*, 2017, **17**, 2765–2770.

30 H. Huang, J. Raith, S. V. Kershaw, S. Kalytchuk, O. Tomanec, L. Jing, A. S. Susha, R. Zboril and A. L. Rogach, *Nat. Commun.*, 2017, **8**, 996.

31 S. Y. Lee, G. Lee, D. Y. Kim, S. H. Jang, I. Choi, J. Park, H.-K. Park, J. W. Jung, K. H. Cho and J. Choi, *APL Photonics*, 2021, **6**, 056104.

32 X. Wang, W. Li, X. Zhao, J. Fu, G. Zhang, W. Ma, W.-H. Zhang and H. W. Choi, *Appl. Phys. Lett.*, 2022, **120**, 011903.

33 G. R. Yettapu, D. Talukdar, S. Sarkar, A. Swarnkar, A. Nag, P. Ghosh and P. Mandal, *Nano Lett.*, 2016, **16**, 4838–4848.

34 J. Maes, L. Balcaen, E. Drijvers, Q. Zhao, J. De Roo, A. Vantomme, F. Vanhaecke, P. Geiregat and Z. Hens, *J. Phys. Chem. Lett.*, 2018, **9**, 3093–3097.

35 C.-S. Jo, K. Noh, S. H. Noh, H. Yoo, Y. Kim, J. Jang, H. H. Lee, Y.-J. Jung, J.-H. Lee, J. Han, J. Lim and S.-Y. Cho, *ACS Appl. Nano Mater.*, 2020, **3**, 11801–11810.

36 Y. Wang, X. Li, V. Nalla, H. Zeng and H. Sun, *Adv. Funct. Mater.*, 2017, **27**, 1605088.

37 Q. A. Akkerman, G. Rainò, M. V. Kovalenko and L. Manna, *Nat. Mater.*, 2018, **17**, 394–405.

38 J. Ye, M. M. Byranvand, C. O. Martínez, R. L. Z. Hoye, M. Saliba and L. Polavarapu, *Angew. Chem., Int. Ed.*, 2021, **60**, 21636–21660.

39 L.-J. Chen, *RSC Adv.*, 2018, **8**, 18396–18399.

40 Q. Liu, J. Yin, B.-B. Zhang, J.-K. Chen, Y. Zhou, L.-M. Zhang, L.-M. Wang, Q. Zhao, J. Hou, J. Shu, B. Song, N. Shirahata, O. M. Bakr, O. F. Mohammed and H.-T. Sun, *J. Am. Chem. Soc.*, 2021, **143**, 5470–5480.

41 K. M. McCall, C. C. Stoumpos, S. S. Kostina, M. G. Kanatzidis and B. W. Wessels, *Chem. Mater.*, 2017, **29**, 4129–4145.

42 B. Saparov, F. Hong, J.-P. Sun, H.-S. Duan, W. Meng, S. Cameron, I. G. Hill, Y. Yan and D. B. Mitzi, *Chem. Mater.*, 2015, **27**, 5622–5632.

43 K. Peng, L. Yu, X. Min, M. Hu, Y. Yang, S. Huang, Y. Zhao, Y. Deng and M. Zhang, *J. Alloys Compd.*, 2022, **891**, 161978.

44 H. Yin, Q. Kong, R. Zhang, D. Zheng, B. Yang and K. Han, *Sci. China Mater.*, 2021, **64**, 2667–2674.

45 J. Luo, X. Wang, S. Li, J. Liu, Y. Guo, G. Niu, L. Yao, Y. Fu, L. Gao, Q. Dong, C. Zhao, M. Leng, F. Ma, W. Liang, L. Wang, S. Jin, J. Han, L. Zhang, J. Etheridge, J. Wang, Y. Yan, E. H. Sargent and J. Tang, *Nature*, 2018, **563**, 541–545.

46 W. B. Fowler, M. J. Marrone and M. N. Kabler, *Phys. Rev. B: Solid State*, 1973, **8**, 5909–5919.

47 R. Scholz, A. Y. Kobitski, D. R. T. Zahn and M. Schreiber, *Phys. Rev. B: Condens. Matter Mater. Phys.*, 2005, **72**, 1–18.

48 S. Li, J. Luo, J. Liu and J. Tang, *J. Phys. Chem. Lett.*, 2019, **10**, 1999–2007.

49 Y. Zhang, Z. Zhang, W. Yu, Y. He, Z. Chen, L. Xiao, J. Shi, X. Guo, S. Wang and B. Qu, *Adv. Sci.*, 2022, **9**, 2102895.

50 H. Zhao, R. Sun, Z. Wang, K. Fu, X. Hu and Y. Zhang, *Adv. Funct. Mater.*, 2019, **29**, 1902262.

51 Y. Liu, Y. Jing, J. Zhao, Q. Liu and Z. Xia, *Chem. Mater.*, 2019, **31**, 3333–3339.

52 P. Han, X. Mao, S. Yang, F. Zhang, B. Yang, D. Wei, W. Deng and K. Han, *Angew. Chem., Int. Ed.*, 2019, **58**, 17231–17235.

53 F. Locardi, E. Sartori, J. Buha, J. Zito, M. Prato, V. Pinchetti, M. L. Zaffalon, M. Ferretti, S. Brovelli, I. Infante, L. De Trizio and L. Manna, *ACS Energy Lett.*, 2019, **4**, 1976–1982.

54 Q. Hu, G. Niu, Z. Zheng, S. Li, Y. Zhang, H. Song, T. Zhai and J. Tang, *Small*, 2019, **15**, 1903496.

55 D. Manna, T. K. Das and A. Yella, *Chem. Mater.*, 2019, **31**, 10063–10070.

56 M. Gray, J. Majher, T. A. Strom and P. Woodward, *Inorg. Chem.*, 2019, **58**, 13403–13410.

57 N. Shirahata, J. Nakamura, J. Inoue, B. Ghosh, K. Nemoto, Y. Nemoto, M. Takeguchi, Y. Masuda, M. Tanaka and G. A. Ozin, *Nano Lett.*, 2020, **20**, 1491–1498.

58 P. Jing, J. Zheng, M. Ikezawa, X. Liu, S. Lv, X. Kong, J. Zhao and Y. Masumoto, *J. Phys. Chem. C*, 2009, **113**, 13545–13550.

59 K. Wei, Z. Xu, R. Chen, X. Zheng, X. Cheng and T. Jiang, *Opt. Lett.*, 2016, **41**, 3821.

60 S. E. Creutz, E. N. Crites, M. C. D. Siena and D. R. Gamelin, *Nano Lett.*, 2018, **18**, 1118–1123.

61 P. Han, X. Zhang, C. Luo, W. Zhou, S. Yang, J. Zhao, W. Deng and K. Han, *ACS Cent. Sci.*, 2022, **6**, 566–572.

62 L. H. Ahrens, *Geochim. Cosmochim. Acta*, 1952, **2**, 155–169.

63 A. R. Denton and N. W. Ashcroft, *Phys. Rev. A: At., Mol., Opt. Phys.*, 1991, **43**, 3161.

64 S. B. Naghadeh, S. Sarang, A. Brewer, A. Allen, Y.-H. Chiu, Y.-J. Hsu, J.-Y. Wu, S. Ghosh and J. Z. Zhang, *J. Chem. Phys.*, 2019, **151**, 154705.

65 L. Liu, R. Zhao, C. Xiao, F. Zhang, F. Pevere, K. Shi, H. Huang, H. Zhong and I. Sychugov, *J. Phys. Chem. Lett.*, 2019, **10**, 5451–5457.

66 J.-P. Ma, J.-K. Chen, J. Yin, B.-B. Zhang, Q. Zhao, Y. Kuroiwa, C. Moriyoshi, L. Hu, O. M. Bakr, O. F. Mohammed and H.-T. Sun, *ACS Mater. Lett.*, 2020, **2**, 367–375.

67 L. Schade, A. D. Wright, R. D. Johnson, M. Dollmann, B. Wenger, P. K. Nayak, D. Prabhakaran, L. M. Herz, R. Nicholas, H. J. Snaith and P. G. Radaelli, *ACS Energy Lett.*, 2019, **4**, 299–305.

68 J. Luo, S. Li, H. Wu, Y. Zhou, Y. Li, J. Liu, J. Li, K. Li, F. Yi, G. Niu and J. Tang, *ACS Photonics*, 2018, **5**, 398–405.

69 P. Zhang, J. Yang and S.-H. Wei, *J. Mater. Chem. A*, 2018, **6**, 1809–1815.

70 J. Zhang, Y. Yang, H. Deng, U. Farooq, X. Yang, J. Khan, J. Tang and H. Song, *ACS Nano*, 2017, **11**, 9294–9302.

71 Y. Tang, L. Gomez, M. van der Laan, D. Timmerman, V. Sebastian, C.-C. Huang, T. Gregorkiewicz and P. Schall, *J. Mater. Chem. C*, 2021, **9**, 158–163.

72 B. M. Benin, D. N. Dirin, V. Morad, M. Wörle, S. Yakunin, G. Rainò, O. Nazarenko, M. Fischer, I. Infante and M. V. Kovalenko, *Angew. Chem., Int. Ed.*, 2018, **57**, 11329–11333.

73 R. Saran, A. Heuer-Jungemann, A. G. Kanaras and R. J. Curry, *Adv. Opt. Mater.*, 2017, **5**, 1–9.

74 Y. P. Varshni, *Physica*, 1967, **34**, 149–154.

75 M. Leroux, N. Grandjean, B. Beaumont, G. Nataf, F. Semond, J. Massies and P. Gibart, *J. Appl. Phys.*, 1999, **86**, 3721–3728.

76 A. Al Salman, A. Tortschanoff, M. B. Mohamed, D. Tonti, F. van Mourik and M. Chergui, *Appl. Phys. Lett.*, 2007, **90**, 093104.

77 H. C. Woo, J. W. Choi, J. Shin, S. H. Chin, M. H. Ann and C. L. Lee, *J. Phys. Chem. Lett.*, 2018, **9**, 4066–4074.

78 E. M. Janke, N. E. Williams, C. She, D. Zherebetskyy, M. H. Hudson, L. Wang, D. J. Gosztola, R. D. Schaller, B. Lee, C. Sun, G. S. Engel and D. V. Talapin, *J. Am. Chem. Soc.*, 2018, **140**, 15791–15803.

79 L. Wang, W. Zheng, F. Vitale, X. Zhang, X. Li, Y. Ji, Z. Liu, O. Ghaebi, C. T. Plass, R. Domes, T. Frosch, G. Soavi, E. Wendler, Y. Zhang and C. Ronning, *Adv. Funct. Mater.*, 2022, **32**, 2111338.

80 V. Türck, S. Rodt, O. Stier, R. Heitz, R. Engelhardt, U. W. Phol, D. Bimberg and R. Steingrüber, *Phys. Rev. B: Condens. Matter Mater. Phys.*, 2000, **61**, 9944–9947.

81 X. Lao, Z. Yang, Z. Su, Z. Wang, H. Ye, M. Wang, X. Yao and S. Xu, *Nanoscale*, 2018, **10**, 9949–9956.

82 J. E. Parks, Department of Physics and Astronomy, The University of Tennessee, Tech. Rep., 2013.